RSC Advances

PAPER

View Article Online
View Journal | View Issue

Cite this: *RSC Adv.*, 2017, 7, 28438

Site selective substitution and its influence on photoluminescence properties of $Sr_{0.8}Li_{0.2}Ti_{0.8}Nb_{0.2}O_3:Eu^{3+}$ phosphors†

G. Jyothi,[ab] L. Sandhya Kumari[a] and K. G. Gopchandran *[a]

Received 28th March 2017
Accepted 19th May 2017

DOI: 10.1039/c7ra03598e

rsc.li/rsc-advances

Perovskite red phosphors $Sr_{0.95-x}Eu_{0.05}Li_xTi_{1-x}Nb_xO_3$ ($0 \leq x \leq 0.3$), $Sr_{0.8-x}Li_{0.2}Ti_{0.8}Nb_{0.2}O_3:xEu^{3+}$ ($0 \leq x \leq 0.16$) and $Sr_{0.8-x/2}Li_{0.2}Ti_{0.8-x/2}Nb_{0.2}O_3:xEu^{3+}$ ($0 \leq x \leq 0.16$) were prepared by solid state reaction. The influence of increase of Eu^{3+} concentration and effect of altering substitution sites of Eu^{3+} ions from A-sites to simultaneously at A- and B-sites of the host lattice on the photoluminescence properties of the phosphors were investigated. The site selective substitution of Eu^{3+} ions is described with changes in cell volume obtained from X-ray diffraction patterns, Raman shifts and the decay curve profiles obtained from luminescence life time measurements. From the Raman spectra it is found that simultaneous substitution of Eu^{3+} ions at A- and B-sites increases the intensity of first order TO_2, TO_4 and LO_4 vibrational modes at 184, 541 and 811 cm^{-1} and the first order R-point vibrations at 147, 229 and 449 cm^{-1} significantly, indicating excess defect concentration. The single exponential luminescence decay curves observed for $Sr_{0.8-x}Li_{0.2}Ti_{0.8}Nb_{0.2}O_3:xEu^{3+}$ phosphors reveal A-sites occupancy and the double exponential nature of decay curves of $Sr_{0.8-x/2}Li_{0.2}Ti_{0.8-x/2}Nb_{0.2}O_3:xEu^{3+}$ phosphors confirm the simultaneous occupancy of europium at A- and B-sites. Interestingly we observed a sharp increase in asymmetric ratio between the electric and magnetic dipole transitions $^5D_0 \rightarrow {}^7F_2$ and $^5D_0 \rightarrow {}^7F_1$, from 2.09 to 4.09, on doubling the substitution sites of Eu^{3+} resulting in enhanced color purity. It is found that simultaneous substitution increases the intensity of red emission at 615 nm, under optimum doping conditions, by 1.46 times. Further, from Judd–Ofelt analysis, J–O intensity parameter Ω_2 is found to increase from 3.67×10^{-20} to 4.80×10^{-20} cm^2, on altering substitution of Eu^{3+} from A-sites to A- and B-sites simultaneously, substantiating the increase of local asymmetry in the lattice. The radiative and non-radiative transition rates, radiative life time, branching ratios and stimulated emission cross sections of all these phosphors are also reported. The color coordinates are described with CIE chromaticity diagram. Color purity and color temperature of these phosphors are also described in detail.

1. Introduction

Rare earth elements find a variety of optical applications such as in white light emitting diodes (WLEDs), fluorescent lamps, display devices, photonic devices, solid state lasers, and biological labeling.[1,2] The field of solid state lighting applications like phosphor converted WLEDs is in need of new thermally and chemically stable high quantum yield red phosphors which absorb UV and visible radiations for producing white light of appropriate color rendering index (CRI) and correlated color temperature (CCT).[3] The Eu^{3+} ion is an essential activator for many inorganic lattices to produce orange-red emission by the transitions $^5D_0 \rightarrow {}^7F_J$, $J = 0, 1, 2, 3$.[4] Eu^{3+} can also be used as a structural probe since its absorption and emission spectrum

---

[a] *Department of Optoelectronics, University of Kerala, Thiruvananthapuram-695581, India. E-mail: gopchandran@yahoo.com*

[b] *Department of Physics, M. S. M. College, Kayamkulam-690502, India*

† Electronic supplementary information (ESI) available: Calculation procedure for Judd–Ofelt intensity parameters. Fig. S1, (a) XRD patterns and (b) expanded view of (110) reflection of $Sr_{0.95-x}Eu_{0.05}Li_xTi_{1-x}Nb_xO_3$ phosphors. Fig. S2, Raman spectra of (a) SL_1:$Sr_{0.8-x}Li_{0.2}Ti_{0.8}Nb_{0.2}O_3:xEu^{3+}$ and (b) SL_2: $Sr_{0.8-x/2}Li_{0.2}Ti_{0.8-x/2}Nb_{0.2}O_3:xEu^{3+}$. The DR spectra and inset: $[F(R_\infty)h\nu]^2$ *versus* band gap plots in Fig. S3. Fig. S4 shows excitation spectra of different samples monitored at 615 nm (a) SL_1: $Sr_{0.8-x}Li_{0.2}Ti_{0.8}Nb_{0.2}O_3:xEu^{3+}$ and (b) SL_2: $Sr_{0.8-x/2}Li_{0.2}Ti_{0.8-x/2}Nb_{0.2}O_3:xEu^{3+}$. Fig. S5 shows emission spectra of SL_1:$Sr_{0.8-x}Li_{0.2}Ti_{0.8}Nb_{0.2}O_3:xEu^{3+}$ phosphors under (a) 465 nm and (b) 395 nm excitations. Fig. S6 shows emission spectra of SL_2: $Sr_{0.8-x/2}Li_{0.2}Ti_{0.8-x/2}Nb_{0.2}O_3:xEu^{3+}$ phosphors under (a) 465 nm and (b) 395 nm excitations; insets, the expanded view of $^5D_0 \rightarrow {}^7F_1$ and $^5D_0 \rightarrow {}^7F_2$ transitions for the respective excitations. Fig. S7, emission spectra of $Sr_{0.95-x}Eu_{0.05}Li_xTi_{1-x}Nb_xO_3$ phosphors under 465 nm excitation. Fig. S8, emission spectra of $Sr_{0.8}Li_{0.2}Ti_{0.8}Nb_{0.2}O_3:Eu^{3+}$ phosphors in which Eu^{3+} substituted at Sr and Ti sites at different doping ratio, under 465 nm excitation. The photoluminescence decay curves for $^5D_0$–$^7F_2$ transition (615 nm) of $Sr_{0.8-x}Eu_xLi_{0.2}Ti_{0.8}Nb_{0.2}O_3$ (SL_1) and $Sr_{0.8-x/2}Eu_xLi_{0.2}Ti_{0.8-x/2}Nb_{0.2}O_3$ (SL_2) phosphors under 465 nm excitation in Fig. S9(a) and (b) respectively. Structural parameters and band gap energy of $Sr_{0.8-x}Li_{0.2}Ti_{0.8}Nb_{0.2}O_3:xEu^{3+}$ (SL_1) and $Sr_{0.8-x/2}Li_{0.2}Ti_{0.8-x/2}Nb_{0.2}O_3:xEu^{3+}$ (SL_2) phosphors are presented in Tables S1 and S2. See DOI: 10.1039/c7ra03598e

depends on its site symmetry in the host lattice.[5] In a crystal site with inversion symmetry, the magnetic dipole transition ($^5D_0 \rightarrow {}^7F_1$) of Eu^{3+} (~590–600 nm) is dominant. As the symmetry of site deviates from its ideal form due to the incorporation of a dopant ion or changes in the ligand field surrounding the fluorescing ion, the electric dipole transition ($^5D_0 \rightarrow {}^7F_2$) becomes dominant, which give rise to enhanced red emission (~610–630 nm). An important strategy to achieve excellent luminescence is the selection of a suitable host for the rare earth ion. Perovskite oxides with general formula ABO_3 have been termed as inorganic chameleons because of the flexibility of their structure to accommodate different sized ions by deviating from the cubic structure and thus to exhibit variety of physical and chemical properties. It has already been reported that required property improvement can be obtained by substitution and/or doping of individual and mix ions of varying sizes and valances at A- and B-sites.[6,7] High stability of perovskite structure offers substitution of ions at A and B sites independent of their valances and is exploited by many researchers recently. Crystal chemical tuning in these materials, accomplished through doping of lanthanide ions in both A and B sites induces large change in chemical and physical properties. Tuning bulk electrical properties, photo catalytic water splitting, persistent luminescence, self-activated luminescence and transition metal and rare earth (RE) activated luminescence by controlling the local environment around A- and B-cations in perovskites and other complex oxides is a frontier area of research.[6,8–11] The ideal cubic perovskite structure has smaller cation in 6-fold co-ordination surrounded by an octahedron of anions and larger cations in 12-fold cuboctahedral coordination. $SrTiO_3$ (STO) is an extensively studied cubic perovskite material due to its excellent ferroelectric, magnetic, dielectric, thermoelectric and photocatalytic properties.[11,12] STO can be considered as a good host for RE ions because of its wide band gap, high refractive index and low phonon energy. Doping mechanism experiments done by substituting dopant ions *viz.*, transition metals like Mn^{2+} and rare earths ions of Pr^{3+}, Nd^{3+}, Sm^{3+}, Gd^{3+}, Dy^{3+}, Er^{3+} and Yb^{3+}in A and B sites of STO separately revealed that substituting position has major effect on ferroelectric transition temperature and dielectric behavior.[13,14]

Here, we made an attempt to enhance the photo luminescence properties of $SrTiO_3{:}Eu^{3+}$ by preparing a solid solution host of perovskite compounds $SrTiO_3$ and $LiNbO_3$ (LNO). Solid solution compounds provide new structural possibilities concerning metal ion co-ordination environment. Energy absorption abilities of host material can be tailored by preparing solid solution of mixed valent perovskites through modification of energy band structure for color tuning of emission, enhancing emission intensity to get a better quantum yield and/or for improving chemical stability.[15,16] LNO, a perovskite material with trigonal structure, has very low optical losses and very high value of the main electro-optical coefficient and nonlinear coefficient. They are the most preferred materials for electrically driven light generators, scanners and modulators in integrated optics and most important nonlinear material in photonics.[17] Being a low phonon energy material, LNO can increase the radiative transitions between energy levels.[18] Hence the substitution of LNO is done here with the intension to improve the luminescence properties. We optimized the concentration of LNO as 20 mol%, showing better luminescence properties and phase purity.

In this work $Sr_{0.95-x}Eu_{0.05}Li_xTi_{1-x}Nb_xO_3$ ($x = 0$, 0.05, 0.1, 0.2 and 0.3), $Sr_{0.8-x}Li_{0.2}Ti_{0.8}Nb_{0.2}O_3{:}xEu^{3+}$ ($x = 0.05$, 0.08, 0.12, 0.16, and 0.20) and $Sr_{0.8-x/2}Li_{0.2}Ti_{0.8-x/2}Nb_{0.2}O_3{:}xEu^{3+}$ ($x = 0.05$, 0.08, 0.12, 0.16, and 0.20) were prepared by solid state reaction method. At first, the phosphor was prepared by substituting Eu^{3+} ions at A-sites and then preparation was done by substituting Eu^{3+} ions at A- and B-sites simultaneously. The site selective substitution is done here to explore relationship between the change in photoluminescence properties and alteration of structure around the activator ions. A variety of spectroscopic techniques and X-ray diffraction measurements were used to investigate the influence of site selective substitution. Judd–Ofelt analysis is used to analyze luminescence and radiative properties of phosphors.

2. Experimental section

The perovskite compounds $Sr_{0.95-x}Eu_{0.05}Li_xTi_{1-x}Nb_xO_3$ ($x = 0$, 0.05, 0.1, 0.2 and 0.3), $Sr_{0.8-x}Li_{0.2}Ti_{0.8}Nb_{0.2}O_3{:}xEu^{3+}$ ($x = 0$, 0.05, 0.08, 0.12, 0.16, and 0.20) and $Sr_{0.8-x/2}Li_{0.2}Ti_{0.8-x/2}Nb_{0.2}O_3{:}xEu^{3+}$($x = 0.05$, 0.08, 0.12, 0.16, and 0.20) were synthesized by conventional solid state method using the starting materials Li_2CO_3, $SrCO_3$, TiO_2, Nb_2O_5 and Eu_2O_3 (Sigma Aldrich – 99.99%). The raw materials were mixed in proper stoichiometry and then homogenized by wet mixing with acetone in an agate mortar for 30 min. The products obtained after wet mixing was calcined using alumina crucibles in an electric furnace at the temperature of 1250 °C for 6 hours with intermittent grinding. The heating of the furnace was programmed to increase the temperature initially at 10 °C min^{-1} up to 700 °C and afterwards the heating rate was decreased to 5 °C min^{-1}. The calcined samples were ground to fine powders for further characterizations.

X-ray powder diffraction analysis was performed with diffractometer having Ni filtered Cu-Kα radiation ($\lambda = 1.5405$ Å) varying 2θ from 10 to 90° in 0.02 steps. X'Pert HighScore Plus programme was used for Rietveld refinement of X-ray diffraction patterns for structural analysis. The crystal structure of cubic $SrTiO_3$ with *pm*3*m* space group (no. 221) was used as the starting model for all the samples with A, B and oxygen ions at the Wyckoff sites 1b, 1a and 3d respectively. Raman spectra were recorded in a back scattering geometry using a confocal micro Raman spectrometer system (Horiba Jobin – Yvon LABRAM-HR 800) equipped with a Peltier cooled CCD detector. The elemental analysis and elemental X-ray dot mapping was carried out by FEI-Nova nano SEM 450 field emission scanning electron microscope. Structural properties were analysed by JEOL JEM2100 transmission electron microscope. FTIR transmittance spectra were obtained from JASCO4100 FTIR spectrometer and UV-visible diffuse reflectance spectra from JASCO V-550 spectrophotometer. The photoluminescence spectra and lifetime measurements of samples were obtained by Jobin Yvon FLUOROLOG FL3-11 spectrofluorimeter and the PL measurements of all the prepared phosphors were done at a time by taking equal quantity of samples, to compare luminescence intensity.

3. Results and discussion

3.1 Structural, morphological and photoluminescence studies

Powder XRD patterns of $Sr_{0.95-x}Eu_{0.05}Li_xTi_{1-x}Nb_xO_3$ (x = 0, 0.05, 0.1, 0.2 and 0.3) and $Sr_{0.8-x}Li_{0.2}Ti_{0.8}Nb_{0.2}O_3$:$x$$Eu^{3+}$ [SL_1, A-site substituted] and $Sr_{0.8-x/2}Li_{0.2}Ti_{0.8-x/2}Nb_{0.2}O_3$:$x$$Eu^{3+}$ [SL_2, A- and B-sites simultaneously substituted], with x = 0, 0.05, 0.08, 0.12 and 0.16 of phosphor samples are shown in Fig. S1(a),† 1(a) and (b) respectively. All the X-ray diffraction patterns are indexed according to the JCPDS card no. 89–4934 (space group *pm*3*m*) of cubic strontium titanium oxide. The samples are found to be polycrystalline and no peaks other than that of $SrTiO_3$ were found in these patterns. This indicates that these samples are single phased and substitution of LNO and Eu^{3+} does not activate any significant change in the crystal structure. However in the X-ray diffraction patterns of samples with excess europium, $x > 0.16$, additional peaks corresponding to europium compounds were observed (not shown). The observed peak shifts due to increase in lattice parameter with LNO incorporation (Fig. S1(a)†) in $Sr_{0.95-x}Eu_{0.05}Li_xTi_{1-x}Nb_xO_3$ indicates expansion of unit cell, which is in agreement with the earlier reports.[19] The appearance of small shoulder in the reflection peaks for $x = 0.30$, as evidenced by the expanded view of (110) reflection specifies that the symmetry of crystalline samples lowers from cubic structure when concentration of $LiNbO_3$ exceeds 20 mol% (Fig. S1(b)†). Perovskite structures are stable when RE ions are doped at A- and/or B-sites.[20] Samples SL_1 and SL_2 are prepared considering inclusion of Eu^{3+} ions at A-site and simultaneously both at A- and B-sites respectively. The peak shift observed with different Eu contents, for both type of substitutions is shown in Fig. 1(c) and (d).

In order to detect the modifications on the structural parameters as a result of Eu^{3+} doping, Rietveld analysis of X-ray diffraction patterns of all the samples were done. Fig. 2 shows the best fitted pattern of the observed, calculated and difference curves and the Bragg positions of $Sr_{0.74}Eu_{0.12}Li_{0.2}Ti_{0.74}Nb_{0.2}O_3$ (SL_2c) phosphor. Lattice parameter, unit cell volume, bond distances and *R*-factors of SL_1 and SL_2 type phosphors prepared

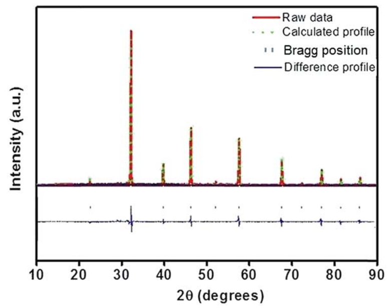

Fig. 2 Rietveld refinement of X-ray diffraction pattern of $Sr_{0.74}Eu_{0.12}Li_{0.2}Ti_{0.74}Nb_{0.2}O_3$ (SL_2c) phosphor.

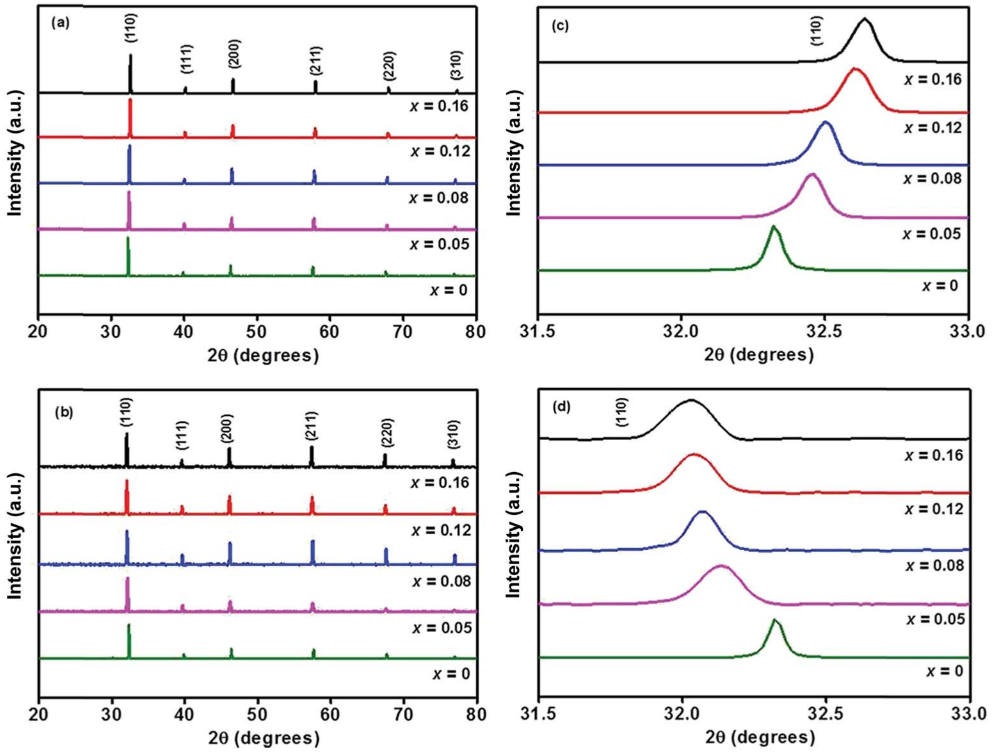

Fig. 1 XRD patterns of (a) $Sr_{0.8-x}Li_{0.2}Ti_{0.8}Nb_{0.2}O_3$:$x$$Eu^{3+}$ (SL_1) and (b) $Sr_{0.8-x/2}Li_{0.2}Ti_{0.8-x/2}Nb_{0.2}O_3$:$x$$Eu^{3+}$ (SL_2) phosphors, expanded view of (110) reflection of (c) SL_1 and (d) SL_2.

with europium content, $x = 0.12$ (SL_1c and SL_2c respectively) for which the luminescence emission intensity was maximum, along with that of $SrTiO_3$ (ST) and $Sr_{0.8}Li_{0.2}Ti_{0.8}Nb_{0.2}O_3$ (SL) are depicted in the Table 1. The structural parameters for all SL_1 and SL_2 phosphors with different compositions is given in Table S1.† The refinements of the samples converges well with the observed XRD patterns only when the site occupancy factor (sof) for Eu at 1b and 1a Wyckoff sites are 100% and 0% respectively for SL_1 phosphors and 50% each at 1b and 1a sites for SL_2 phosphors. This evidences the occupancy ratio of Eu^{3+} ions as 1 : 0 for SL_1 and 1 : 1 for SL_2 phosphors at Sr^{2+} and Ti^{4+} sites. In the case of SL_1, the lattice parameter (a) reduces from 3.9115(1) to 3.9006(1) and cell volume contracts about 0.72% and for SL_2, the lattice parameter increases from 3.9115(1) to 3.9175(1) and unit cell volume expands about 0.57% when europium content is increased from 0 to 16 mol% (Fig. 3). These changes in the cell volume are reflected in the Sr–O and Ti–O bond distances. Considering the ionic radii of Sr^{2+} ions (1.44 Å, CN 12) and Li^+ ions (0.92 Å, CN 8) positioned at the A-sites and Ti^{4+} ions (0.605 Å, CN 6) and Nb^{5+} ions (0.640 Å, CN 6) at B-sites, contraction of unit cell observed for SL_1 proposes the possibility of entering Eu^{3+} ions (0.947 Å, CN 6) in A-site replacing Sr^{2+} ions.[11,21,22] In the case of SL_2, the observed expansion of cell volume is a clear indication of occupancy of Eu^{3+} ions at the sites of smaller Ti^{4+} ions (B-sites) in addition to the most favorable A-site occupancy.[11,19,20] The substitution of Eu^{3+} ions at Nb^{5+} sites is excluded here by considering the fact that concentration of Nb^{5+} is only 4 times less than that of titanium and strontium in these systems.

Fig. 4 shows IR transmittance spectra of the samples $SrTiO_3$ (ST), $Sr_{0.8}Li_{0.2}Ti_{0.8}Nb_{0.2}O_3$ (SL), $Sr_{0.68}Eu_{0.12}Li_{0.2}Ti_{0.8}Nb_{0.2}O_3$ (SL_1c) and $Sr_{0.74}Eu_{0.12}Li_{0.2}Ti_{0.74}Nb_{0.2}O_3$ (SL_2c). Normally observed Ti–O bands in perovskite titanates are in the 200–400 and 540–750 cm^{-1} regions.[23] The broad band in the region 540–750 cm^{-1} corresponds to stretching mode (TO_4) of Ti–O band.[24,25] The IR active Nb–O antisymmetric stretching mode at 550 cm^{-1} and the finger print absorption of $LiNbO_3$ near 677 cm^{-1} are superimposed with the Ti–O band.[26,27] For SL_2c, SL_1c and SL, the absorption at 550 cm^{-1} is clearly visible in the spectra. No impurity peaks are observed in the spectra.

Raman spectroscopic analysis is used to determine substitution positions of europium ions in the samples. Raman spectra of $Sr_{0.8-x}Li_{0.2}Ti_{0.8}Nb_{0.2}O_3{:}xEu^{3+}$ [SL_1, A-site substituted] and $Sr_{0.8-x/2}Li_{0.2}Ti_{0.8-x/2}Nb_{0.2}O_3{:}xEu^{3+}$ [SL_2, A- and B-sites simultaneously substituted] samples are shown in Fig. S2(a) and (b)† respectively. Fig. 5 shows the Raman spectra of SL_2c, SL_1c, SL and ST. The irreducible representation of optical phonon modes of cubic perovskite with $O_h^1(m3m)$ space group is

$$\Gamma = 3F_{1u} + F_{2u} \tag{1}$$

where F_{1u} species are allowed in infrared (IR) only and F_{2u} is forbidden in IR and Raman. Therefore no first order Raman scattering is expected, according to factor group symmetry analysis.[28,29] The presence of first order Raman modes along with the second order broad bands at 210–560 and 600–900 cm^{-1} regions of pure ST sample evidences the breakdown of symmetry selection rules.[30–32] To preserve electro neutrality, creation of oxygen vacancies and distortion of structure occurs, when Eu^{3+} ions are incorporated in the crystal system. Presence of impurity atoms and oxygen vacancies in the system may relax the first order symmetry principles and make the fundamental phonon modes, Slater-type (TO_1/LO_1), last-type (TO_2/LO_2) and axe-type (TO_4/LO_4) to appear.[32] In ABO_3, B ion motion against oxygen vibrations give rise to lowest frequency TO_1/LO_1 modes. Vibrations of A ions result in TO_2/LO_2 mid frequency modes. High frequency TO_4/LO_4 modes are due to oxygen vibrations in BO_6 octahedra.[33] Polar nature of these modes is responsible for their broadness in the Raman spectra.[34]

Table 1 Structural parameters of $SrTiO_3$ (ST), $Sr_{0.8}Li_{0.2}Ti_{0.8}Nb_{0.2}O_3$ (SL), $Sr_{0.68}Eu_{0.12}Li_{0.2}Ti_{0.8}Nb_{0.2}O_3$ (SL_1c) and $Sr_{0.74}Eu_{0.12}Li_{0.2}Ti_{0.74}Nb_{0.2}O_3$ (SL_2c)

Sample	STO	SL	SL_1c	SL_2c
a (Å)	3.9036(2)	3.9115(1)	3.9021(1)	3.9159(1)
V (Å^3)	59.48	59.78	59.41	60.05
R_p (%)	13.18	11.29	13.76	12.19
R_{wp} (%)	15.16	12.89	15.86	15.21
χ^2 (%)	1.9	1.6	1.6	1.5
Sr–O (Å)	2.7600(1)	2.7660(1)	2.7590(2)	2.7690(2)
Ti–O (Å)	1.9520(1)	1.9550(1)	1.9510(2)	1.9580(2)

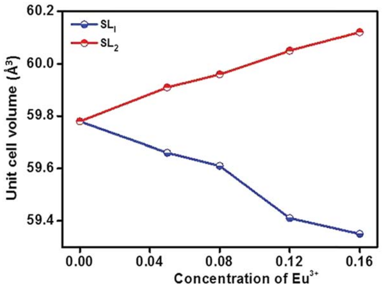

Fig. 3 Variation of unit cell volume for $Sr_{0.8-x}Li_{0.2}Ti_{0.8}Nb_{0.2}O_3{:}xEu^{3+}$ (SL_1) and $Sr_{0.8-x/2}Li_{0.2}Ti_{0.8-x/2}Nb_{0.2}O_3{:}xEu^{3+}$ (SL_2) as a function of concentration of Eu^{3+}.

Here substitution of Eu^{3+} ions and the change of substitution positions alter the frequency and the intensity of observed Raman modes. Variation of intensity and frequency of Raman modes and appearance of new modes due to substitution of

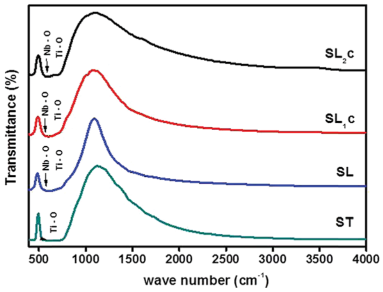

Fig. 4 FTIR transmittance spectra of $SrTiO_3$ (ST), $Sr_{0.8}Li_{0.2}Ti_{0.8}Nb_{0.2}O_3$ (SL), $Sr_{0.68}Eu_{0.12}Li_{0.2}Ti_{0.8}Nb_{0.2}O_3$ (SL_1c) and $Sr_{0.74}Eu_{0.12}Li_{0.2}Ti_{0.74}Nb_{0.2}O_3$ (SL_2c).

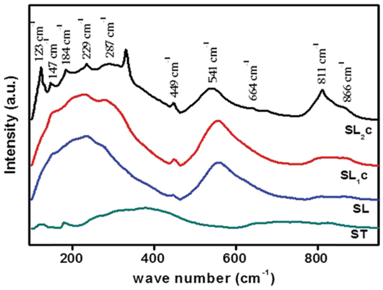

Fig. 5 Raman spectra of $SrTiO_3$ (ST), $Sr_{0.8}Li_{0.2}Ti_{0.8}Nb_{0.2}O_3$ (SL), $Sr_{0.68}Eu_{0.12}Li_{0.2}Ti_{0.8}Nb_{0.2}O_3$ (SL_1c) and $Sr_{0.74}Eu_{0.12}Li_{0.2}Ti_{0.74}Nb_{0.2}O_3$ (SL_2c) phosphors.

Eu^{3+} at A- and simultaneously at both A- and B-sites are studied by de-convolution of the observed Raman spectra (Fig. 6). Raman modes other than second order modes observed for the four samples, $SrTiO_3$ (ST), $Sr_{0.8}Li_{0.2}Ti_{0.8}Nb_{0.2}O_3$ (SL), $Sr_{0.68}Eu_{0.12}Li_{0.2}Ti_{0.8}Nb_{0.2}O_3$ (SL_1c) and $Sr_{0.74}Eu_{0.12}Li_{0.2}Ti_{0.74}Nb_{0.2}O_3$ (SL_2c) are represented in the Table 2. For $SrTiO_3$, fundamental type first order modes are observed at 122 (TO_1), 180 (TO_2), 562 (TO_4), and 758 cm^{-1} (LO_4) and a mode due to tetragonal distortion at 151 cm^{-1}.[29,32,35] For $Sr_{0.8}Li_{0.2}Ti_{0.8}Nb_{0.2}O_3$, corresponding modes are observed at 120 (TO_1), 189 (TO_2), 551 (TO_4) and 807 cm^{-1} (LO_4). The observed increase in intensity of Raman shift due to TO_2 mode arises from incorporation of Li^+ at A-sites, affecting vibrations of Sr^{2+} ions. The additional mode appeared at 447 cm^{-1} is from the first order vibrations of R-point of the Brillouin zone, which can be due to tetragonal distortion.[36] This distortion in the frame work, resulted from the tilting of TiO_6 octahedra on the addition of Li and Nb, deviates the tolerance factor of crystal structure from unity. Additional band at 267 (A_1 (TO_1)) and 876 cm^{-1} (E (LO)) are the first order bending modes of Nb–O–Nb linkage and the stretching vibrations of Nb–O bond respectively.[29,37] A_1 (TO_1) and E (LO) are the active modes of $LiNbO_3$ ($R3c$ space group), which optical phonon modes are expressed by irreducible representation as,

$$\Gamma_{\text{optical}} = 4A_1 + 5A_2 + 9E \quad (2)$$

where A_2 modes are Raman inactive.[38,39] In the case of SL_1c, augmentation of intensities of modes at 449 and 813 cm^{-1} is a clear indication of enhanced local distortions in the lattice due to Eu incorporation at the A-sites.[22] For SL_2c, increased intensity of mode at 123 cm^{-1} (TO_1) specifies incorporation of Eu^{3+} at B-(Ti^{4+}) sites. This mode is related to Ti–O–Ti bending. Here the octahedral tilting occurred as a result of the substitution of larger Eu^{3+} at smaller B-sites alter Ti–O–Ti vibrations to arise first order TO_1 mode. Intensity enhancement of first order TO_2, TO_4 and LO_4 modes at 184 and 541 and 811 cm^{-1} respectively and first order R-point vibrations at 147, 229 and 449 cm^{-1}, is an indication of increase of defect concentration, due to doping at B-sites.[22] The new band at 487 cm^{-1}, assigned as the LO_2 mode can be attributed to vibrations of Sr^{2+}.[33] Difference combinations and additive combinations contribute to new modes at 332 and 664 cm^{-1} respectively.[22,29] Intensity enhancement of Ti–O vibration mode (LO_4) in pure strontium titanate suggests presence of impurities or oxygen vacancies at B-site according to earlier reports.[28] In order to find change in intensity of LO_4 mode at 811 cm^{-1} with respect to doping, ratio of intensities (I_{LO_4}/I_{600}) is calculated between that of LO_4 mode and the second order mode at 600 cm^{-1}, which is having significant intensity and no shift in position. Remarkable increase in the intensity ratio I_{LO_4}/I_{600} (Table 2) for double site Eu doped phosphor further evidences increased polar defects created by incorporation of larger Eu^{3+} ions instead of smaller Ti^{4+} ions of different valance at the B-site in addition to the substitution at A-site.[40] In earlier reports, even though tetragonal local distortion was confirmed by vibrational spectroscopy, no evidence of tetragonal phase was confirmed by XRD analysis for the samples heavily doped with rare earth elements.[13,32] This is in agreement with the results obtained in our work.

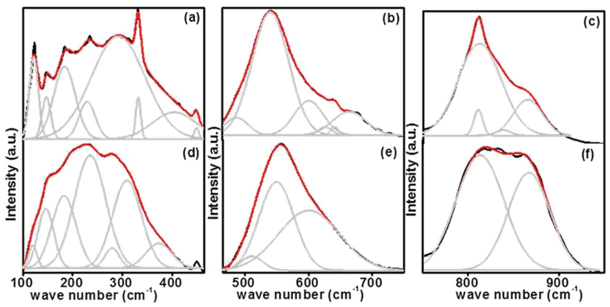

Fig. 6 Deconvoluted Raman spectra of $Sr_{0.74}Eu_{0.12}Li_{0.2}Ti_{0.74}Nb_{0.2}O_3$ (SL_2c) in the range 100–460 (a), 460–750 (b), 750–950 cm^{-1} (c) and that of $Sr_{0.68}Eu_{0.12}Li_{0.2}Ti_{0.8}Nb_{0.2}O_3$ (SL_1c) in the range 100–460 (d), 460–750 (e), 750–950 cm^{-1} (f).

To understand elemental composition and distribution of each element in the phosphors, EDX analysis of $Sr_{0.8-x}Eu_x$-$Li_{0.2}Ti_{0.8}Nb_{0.2}O_3$ (SL_1c) and $Sr_{0.74}Eu_{0.12}Li_{0.2}Ti_{0.74}Nb_{0.2}O_3$ (SL_2c) were done and found to be composed of elements Sr, Ti, Nb, Eu and O. Corresponding EDX spectra are shown in Fig. 7. Quantitative EDX analysis shows increase of concentration of Sr and decrease of concentration of Ti in SL_2c in comparison with SL_1c, while other elements remain almost unaltered, in accordance with the theoretical stoichiometry (Table 3). This demonstrates that in SL_1c, Eu^{3+} ions are substituted at Sr^{2+} sites whereas in SL_2c, the substitution of Eu^{3+} takes place both at Sr^{2+} and Ti^{4+} sites simultaneously and supports the fact that Nb^{5+} sites are almost undisturbed in the phosphor systems. Elemental X-ray dot mapping images show that constituent elements are equally distributed in the samples (Fig. 8).

The TEM images and the SAED pattern of SL_2c phosphor is shown in Fig. 9. The images show the crystalline nature of the phosphor and the obtained lattice spacing of 0.28 nm is in agreement the X-ray diffraction analysis.

The diffuse reflectance spectra of $SrTiO_3$ (ST), $Sr_{0.8}Li_{0.2}$-$Ti_{0.8}Nb_{0.2}O_3$ (SL), $Sr_{0.68}Eu_{0.12}Li_{0.2}Ti_{0.8}Nb_{0.2}O_3$ (SL_1c) and $Sr_{0.74}Eu_{0.12}Li_{0.2}Ti_{0.74}Nb_{0.2}O_3$ (SL_2c) show a broad band in the UV-visible region, 220–450 nm with maximum absorbance at 350 nm, which can be attributed to the charge transfer transition from the oxygen ligand to the central titanium, europium and niobium in metal oxygen octahedra (Fig. S3†). In

Table 2 Raman shifts obtained from Raman spectra of $SrTiO_3$ (ST), $Sr_{0.8}Li_{0.2}Ti_{0.8}Nb_{0.2}O_3$ (SL), $Sr_{0.68}Eu_{0.12}Li_{0.2}Ti_{0.8}Nb_{0.2}O_3$ (SL_1c) and $Sr_{0.74}Eu_{0.12}Li_{0.2}Ti_{0.74}Nb_{0.2}O_3$ (SL_2c)

Sample	TO_1 (cm^{-1})	TO_2 (cm^{-1})	LO_2 (cm^{-1})	TO_4 (cm^{-1})	LO_4 (cm^{-1})	Nb–O modes (cm^{-1})	R-Point modes (cm^{-1})	I_{LO_4}/I_{600}
ST	124	180	—	562	758	—	151	—
SL	120	189	—	551	807	277, 865	143, 447	0.44
SL_1	120	182	—	550	813	235, 280, 867	146, 449	0.46
SL_2	123	184	487	541	811	235, 287, 866	147, 229, 449	2.01

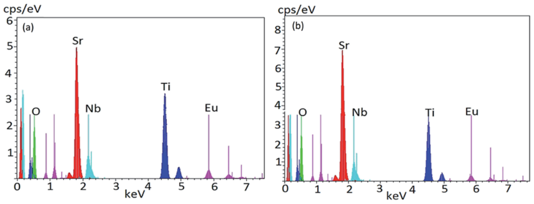

Fig. 7 EDX spectra of (a) $Sr_{0.68}Eu_{0.12}Li_{0.2}Ti_{0.8}Nb_{0.2}O_3$ (SL_1c) and (b) $Sr_{0.74}Eu_{0.12}Li_{0.2}Ti_{0.74}Nb_{0.2}O_3$ (SL_2c) phosphors.

addition to the charge transfer band, small peaks at 465 and 525 nm observed in the spectra of SL_1c and SL_2c are due to the intra 4f transition of Eu^{3+} ion. Kubelka–Munk method was used to calculate band gap energy of samples from diffuse reflectance spectra.[41] Kubelka–Munk function $F(R_\alpha)$ is related to R_α as

$$F(R_\alpha) = \frac{(1 - R_\alpha)^2}{2R_\alpha} = \frac{K}{S} \tag{3}$$

where $R_\alpha = R_{\text{sample}}/R_{\text{reference}}$, K is the absorption coefficient and S, the scattering coefficient. Tauc equation relates band gap E_g and linear absorption coefficient α as

$$\alpha h\nu = C_1\left(h\nu - E_g\right)^{\frac{n}{2}} \tag{4}$$

where ν is the frequency of photon, C_1 is the proportionality constant and for direct allowed transitions, $n = 1$. When there is perfect diffuse scattering, $K = 2\alpha$ and considering S as a constant over the wavelength of measurement, from the above two equations, we can write,

$$[F(R_\alpha)h\nu]^2 = C_2[h\nu - E_g] \tag{5}$$

From $[F(R_\alpha)h\nu]^2$ *versus* $h\nu$ plot, energy gap was found out by extrapolating linear fitted portion of the curve to $[F(R_\alpha)h\nu]^2 = 0$ (Fig. S3†). The band gap energy of SL1 and SL_2 type phosphors are demonstrated in the Table S2.† The obtained values of band gap are comparable with the reported value for $SrTiO_3$.[42]

The photoluminescence excitation spectra of $Sr_{0.8-x}Li_{0.2}Ti_{0.8}Nb_{0.2}O_3$:$x$$Eu^{3+}$ [SL_1, A-site substituted] and $Sr_{0.8-x/}$

Table 3 Quantitative EDX analysis data of $Sr_{0.68}Eu_{0.12}Li_{0.2}Ti_{0.8}Nb_{0.2}O_3$ (SL_1c) and $Sr_{0.74}Eu_{0.12}Li_{0.2}Ti_{0.74}Nb_{0.2}O_3$ (SL_2c) phosphors

	SL_1c: $Sr_{0.68}Eu_{0.12}Li_{0.2}Ti_{0.8}Nb_{0.2}O_3$		SL_2c: $Sr_{0.74}Eu_{0.12}Li_{0.2}Ti_{0.74}Nb_{0.2}O_3$	
Element	Wt%	At%	Wt%	At%
Sr L	29.72	11.51	33.89	12.88
O K	32.04	67.94	33.61	69.95
Ti K	22.75	16.12	19.14	13.31
Nb L	6.86	2.50	6.71	2.41
Eu L	8.62	1.92	6.65	1.46

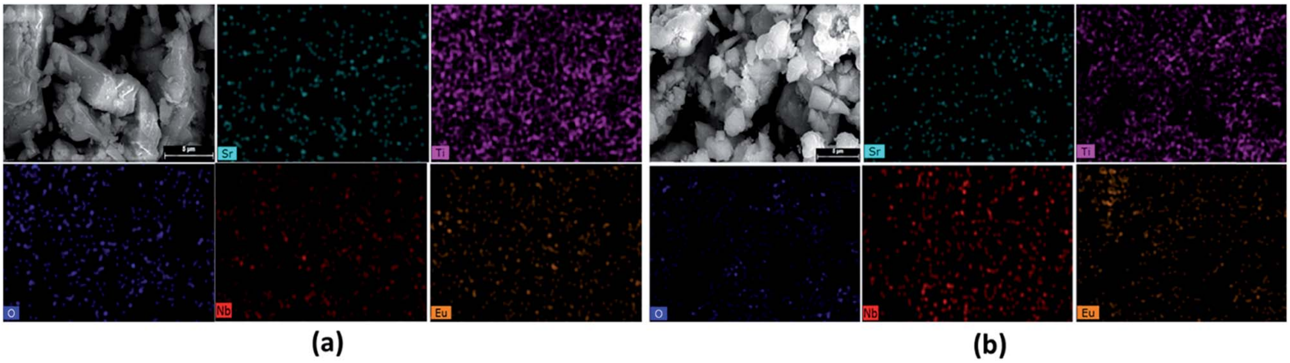

Fig. 8 Elemental X-ray dot mapping images of (a) SL_1c: $Sr_{0.68}Eu_{0.12}Li_{0.2}Ti_{0.8}Nb_{0.2}O_3$ and (b) SL_2c: $Sr_{0.74}Eu_{0.12}Li_{0.2}Ti_{0.74}Nb_{0.2}O_3$ phosphors.

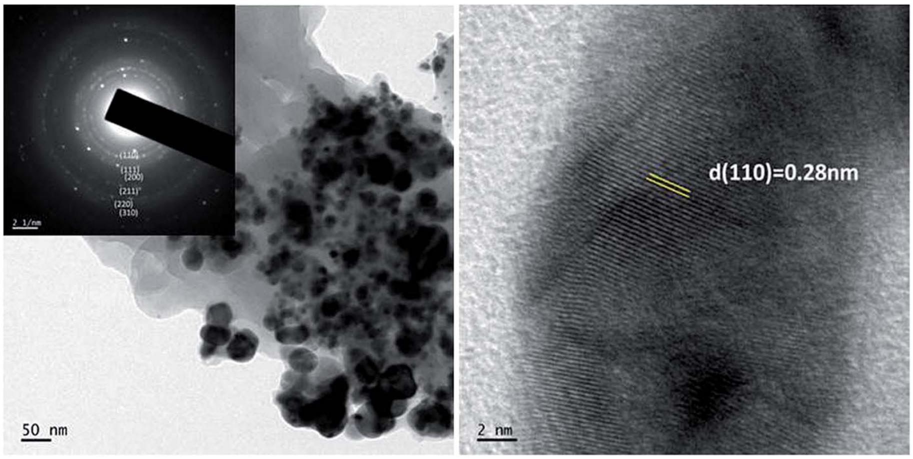

Fig. 9 The TEM images of $Sr_{0.74}Eu_{0.12}Li_{0.2}Ti_{0.74}Nb_{0.2}O_3$ (SL_2c) and inset shows SAED image.

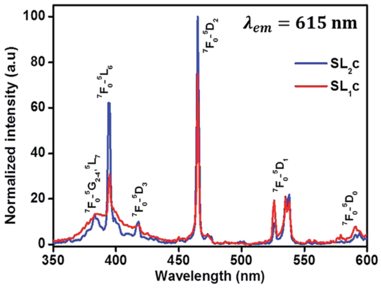

Fig. 10 Excitation spectra of samples with optimum Eu^{3+} concentration of SL_1 type (SL_1c) and SL_2 type (SL_2c) phosphors monitored at 615 nm, normalized with respect to the highest intensity of SL_2c.

$_2Li_{0.2}Ti_{0.8-x/2}Nb_{0.2}O_3$:$x$$Eu^{3+}$ [SL_2, A- and B-sites simultaneously substituted] solid solutions with x varying from 0.05 to 0.16 are shown in Fig. S4 ((a) and (b) respectively)† and the normalized curves of samples with optimum Eu^{3+} concentration is shown in Fig. 10. In all these spectra, a broad charge transfer band (CTB) is present in the region from 350 to 445 nm. The sharp peaks in the spectra at 382, 395, 418, 465, 538 and 590 nm are due to the intra f–f transitions $^7F_0 \rightarrow {}^6G_{2-4}$, $^5L_7$, $^7F_0 \rightarrow {}^5L_6$, $^7F_0 \rightarrow {}^5D_3$, $^7F_0 \rightarrow {}^5D_2$, $^7F_0 \rightarrow {}^5D_1$ and $^7F_0 \rightarrow {}^5D_0$ respectively of Eu^{3+} ions.[43] The CTB is a combined effect of electronic transition from 2p orbital of O^{2-} ions to central metal ions in metal–oxygen polyhedra. The position of CTB depends on covalence between O^{2-} ion and central metal ion, oxygen–metal bond length and coordination number of metal ion.[44] The band for $O_{2p} \rightarrow Eu_{4f}$ and $O_{2p} \rightarrow Nb_{4d}$ charge transfer transitions usually lie in the regions 250–300 and 250–310 nm.[4,43] The observed CTB with low intensity in the region 350 to 450 nm is in agreement with the other reports on $SrTiO_3$:Eu based phosphors.[11,45] Similarly, for $CaTiO_3$:Eu phosphor systems also a low intense CTB was observed in the region 370–410 nm, overlapped with f–f transitions.[46,47] In complex hosts, the contributions from more than one component in the CTB cannot be resolved due to spectral overlap.[48] The absence of O^{2-}–Eu^{3+} CTB may be due to the possible overlap of charge transfer transition $O_{2p} \rightarrow Eu_{4f}$ with $O_{2p} \rightarrow Ti_{3d}$ and $O_{2p} \rightarrow Nb_{4d}$. The attraction of europium ions towards electron clouds of oxygen ions and the resulting polarisation of europium octahedral will be different for different host matrices. Weak attraction between Eu^{3+} ions and electron clouds of oxygen ions decreases the probability of mixing of f-orbitals of Eu^{3+} and p orbitals of O^{2-} and the occurrence of high intense CT transition.[49] The enhanced f–f transitions at 382 and 418 nm in the excitation spectra of SL_2 samples, when compared with SL_1, signify the influence of substitution sites of Eu^{3+} (Fig. 7). For all samples the most intense absorption is at 465 nm and the other prominent absorption peak in the spectra is at 395 nm. The relative intensity of absorption at 465 nm increases with europium concentration, compared to the absorption at 395 nm. The photoluminescence spectra of SL_1 and SL_2 type phosphors under these wavelengths are shown in Fig. S5 and S6† respectively.

Emission from a lanthanide ion occurs due to magnetic dipole transition and electric dipole transition and the probability of transitions is determined by the symmetry of crystal lattice. All the emission spectra obtained in this investigation show mainly two peaks at 593 and 615 nm. However, the substitution of Eu^{3+} at Sr^{2+} sites and simultaneously at Sr^{2+} and Ti^{4+} sites makes the hyper sensitive electric dipole transition $^5D_0 \rightarrow {}^7F_2$ observed at 615 nm to dominate over the $^5D_0 \rightarrow {}^7F_1$ magnetic dipole transition at 593 nm. The variation of site

Table 4 Asymmetric ratio (R_{21}) calculated from emission spectra for $Sr_{0.95-x}Eu_{0.05}Li_xTi_{1-x}Nb_xO_3$, $Sr_{0.8-x}Li_{0.2}Ti_{0.8}Nb_{0.2}O_3$:$x$$Eu^{3+}$ (SL_1) and $Sr_{0.8-x/2}Li_{0.2}Ti_{0.8-x/2}Nb_{0.2}O_3$:$x$$Eu^{3+}$ (SL_2) phosphors at 465 nm excitation

Value of x	Asymmetric ratio (R_{21})	Value of x	Asymmetric ratio (R_{21})	
	$Sr_{0.95-x}Eu_{0.05}Li_xTi_{1-x}Nb_xO_3$		SL_1	SL_2
0	1	0.08	2.03	3.89
0.1	1.36	0.12	2.09	4.09
0.2	1.58	0.16	2.05	3.92
0.3	1.56	—	—	—

symmetry of Eu^{3+} ions can be determined from the evolution of integrated emission intensity ratio of $(^5D_0 \rightarrow {}^7F_2)$ to $(^5D_0 \rightarrow {}^7F_1)$ transition, the asymmetric ratio R_{21}. High value of asymmetry ratio (Table 4) indicates the occupancy of Eu^{3+} ions in non-centro symmetric sites.[50] Larger the asymmetric ratio, closer is the optimal value of color chromaticity. Asymmetric ratio calculated for SL_1 and SL_2 phosphors indicates that there is reduction in the symmetry with the simultaneous substitution of Eu^{3+} at A- and B-sites. The presence of multiplets in the emission spectra of SL_1 type phosphors, corresponding to $^5D_0 \rightarrow {}^7F_4$ (681, 692 and 704 nm) transition are attributed to the partial lifting of degeneracy at the level $J = 4$ due to $2J + 1$ Stark splitting.

The luminescence properties are strongly affected by the host lattice environment of Eu^{3+} activators. Intensive investigations on the influence of substitution of LNO in STO at various compositions and with varying concentrations of Eu^{3+} have been conducted initially. The doping concentration of Eu^{3+} in $SrTiO_3$ is optimized as 5 mol% in earlier reports.[11] Thus the typical photoluminescence of 5 mol% Eu^{3+} doped STO with LNO varying from 0 to 30 mol% is studied to optimize LNO concentration in samples and the corresponding emission spectra are shown in the Fig. S7.† The luminescence intensity increases as the concentration of LNO varies from $x = 0$ to 0.2, and then decreases. This is accompanied by the enhancement asymmetric ratio from 1 to 1.58 as shown in Table 4. The reasons for enhancement in PL properties due to LNO substitution is explained as follows. It has already been reported that for $SrTiO_3$:xEu phosphor, emission due to magnetic dipole transition and electric dipole transition have almost comparable intensity, and is in agreement with that obtained in our work.[11,51] This clearly manifests the change in local coordination around europium ions when perovskite $Sr_{1-x}Eu_xTiO_3$ is substituted with Li^+ and Nb^{5+}. The incorporation of Li^+ and Nb^{5+} ions in the sites of Sr^{2+} and Ti^{4+} ions having different ionic radii and valance may prompt a structural adjustment in such a way as to enhance luminescence properties up to 20 mol% of LNO concentration. Here the substitution of LNO does not create quenching defects due to charge imbalance since the excess charge created by Li^+ substitution is compensated by Nb^{5+} ions. Also, the low phonon nature of LNO may enhance the radiative properties in the system. The departure from cubic symmetry, as confirmed from XRD analysis may result in the luminescence quenching in the system when concentration of LNO exceeds 20 mol%. The PL spectra of SL_1 and SL_2 type phosphors prepared with europium content, $x = 0.12$ (SL_1c and SL_2c respectively) for which the luminescence emission intensity was maximum, along with the spectrum of $Sr_{0.95}Eu_{0.05}TiO_3$ is shown in Fig. 11. This figure evidences the interesting feature of this work, *viz.*, increase in the intensity of red emission and the asymmetric ratio of electric dipole transition $^5D_0 \rightarrow {}^7F_2$ to magnetic dipole transition $^5D_0 \rightarrow {}^7F_1$ as a consequence of substitution of Eu^{3+} at A sites and simultaneously at A and B sites in $Sr_{0.8}Li_{0.2}Ti_{0.8}Nb_{0.2}O_3$ when compared with that of strontium titanate.

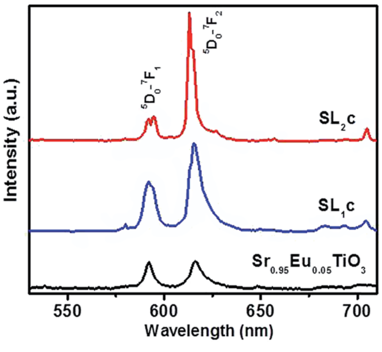

Fig. 11 Comparison of emission spectra of $Sr_{0.95}Eu_{0.05}TiO_3$, $Sr_{0.68}Eu_{0.12}Li_{0.2}Ti_{0.8}Nb_{0.2}O_3$ (SL_1c) and $Sr_{0.74}Eu_{0.12}Li_{0.2}Ti_{0.74}Nb_{0.2}O_3$ (SL_2c).

Comparison of emission from SL_2c and SL_1c phosphors under 465 nm excitation is presented in the Fig. 12(a). The red emission peak becomes sharper and more intense with a change of peak wavelength from 615 to 613 nm as the substitution of Eu^{3+} is done at both A- and B-sites instead of at A-sites alone. Here the intensity enhances 1.46 times and FWHM decreases from 7.34 to 3.99 nm. A similar behavior of both increase of intensity of red emission and color purity can be observed for emissions under 395 nm excitation also (Fig. 12(b)). The enhancement of luminescence properties for the samples in which Eu^{3+} ions are substituted simultaneously both at A- and B-sites can be attributed to the following factors. The substitution of larger Eu^{3+} ions for smaller Ti^{4+} ions results in increased defect concentration at the B-sites in SL_2 type phosphors leading to the local tetragonal distortion due to octahedral tilting, as evidenced by Raman spectra. This increase in local asymmetry favors the enhancement of luminescence properties. Achieving a balance between the number of Sr^{2+} and Ti^{4+} sites replaced by Eu^{3+} ions can lead to a state of valance compensation. This charge compensation in the crystal system is of prime importance in the enhancement of luminescence from phosphors.[52,53] A splitting of $^5D_0 \rightarrow {}^7F_1$ and $^5D_0 \rightarrow {}^7F_2$ emission lines into two is observed for SL_2 phosphors (Fig. 12 and S6†). This suggests the presence of two nonequivalent crystallographic Eu^{3+} sites in these samples since it was not observed for samples with Eu^{3+} substituted exclusively at A-sites.[54]

Initially we have carried out a detailed investigation into the luminescence properties of $Sr_{0.8}Li_{0.2}Ti_{0.8}Nb_{0.2}O_3$:Eu with varying degree of Eu^{3+} substitution at Sr and Ti sites. The emission spectra of the phosphors, under 465 nm excitation with Eu^{3+} at Sr^{2+} and Ti^{4+} sites in the ratio 1 : 0, 0.8 : 0.2, 0.67 : 0.33 and 1 : 1 is shown in Fig. S8† and it indicates that the optimum doping ratio is 1 : 1. It has already been reported that perovskite materials exhibit a limit for B-site doping.[22] In this work, it is found that doping of Eu^{3+} at Ti sites beyond 50% results in formation of additional phases of $Eu_3Ti_2O_7$ and $SrCO_3$. Hence, for obtaining single phase red phosphors, we have limited occupancy ratio of Eu^{3+} to 1 : 1.

Photoluminescence emission intensity enhances nearly 6 times as the concentration of Eu ions in the prepared SL_1 type phosphors increases from 5 mol% to 12 mol%, as shown in the Fig. S5,† beyond which it decreases. A similar trend is observed for SL_2 type phosphors (Fig. S6†). This quenching of

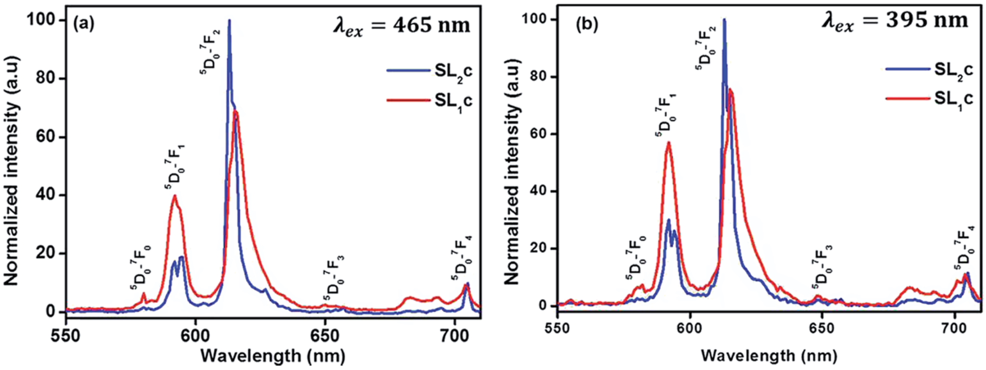

Fig. 12 Emission spectra of $Sr_{0.68}Eu_{0.12}Li_{0.2}Ti_{0.8}Nb_{0.2}O_3$ (SL$_1$c) and $Sr_{0.74}Eu_{0.12}Li_{0.2}Ti_{0.74}Nb_{0.2}O_3$ (SL$_2$c) under the excitation of (a) 465 nm and (b) 395 nm, normalized with respect to the highest intensity of SL$_2$c.

luminescence is observed because of the cross-relaxation mechanism between Eu^{3+} ions. The rate of non radiative energy transfer is high in systems with high dopant concentration. In cross relaxation mechanism, a fraction of excitation energy absorbed by an activator is transferred to another identical ion. As the concentration of the activators increases, the effective distance between them decreases. According to Blasse,[55] the critical distance between dopant ions for energy transfer can be calculated as

$$R_c = 2\left[\frac{3V}{4\pi x_c N}\right]^{1/3} \quad (6)$$

where V is the volume of unit cell, x_c is the critical ion concentration and N is the number of Z ions in the unit cell. In the case of SL$_1$ type phosphors, the estimated value of R_c is 17.74 Å, for which $V = 58.43$ Å^3, $x_c = 0.02$ and $N = 1$. The estimated value of R_c for SL$_2$ is 18.06 Å. Generally there are three mechanisms for non-radiative energy transfer namely, radiation reabsorption, exchange interaction and electrostatic multipolar interaction. For radiation reabsorption to occur fluorescence and absorption spectra should overlap and it is not possible in this case. The Eu^{3+} ions must be very close to each other *i.e.*; a distance of separation of 6 Å or less is needed for the exchange interaction to take place.[1] The values for R_c obtained here rejects the chance of overlap of donor and acceptor ion charge distribution. As a result we can infer that the electrostatic multipolar interaction is the major mechanism which brings about the concentration quenching in this case.

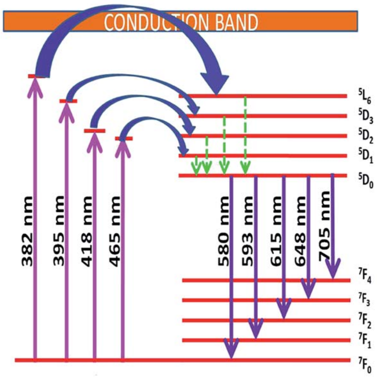

Fig. 13 Schematic energy level diagram showing possible transitions of Eu^{3+} activator ion in the host matrix.

Energy level diagram of all possible transitions considering excitation and emission spectra is presented in the Fig. 13. The color coordinates (x, y), correlated color temperature and color purity calculated from the emission spectra under 465 nm excitation for the phosphors are depicted in the Table 5. The chromaticity coordinates calculated using CIE 1931 color matching functions[56] indicate that all the phosphors have red emission. The CIE 1931 chromaticity diagram and correlated color temperature diagram of the prepared SL$_1$ and SL$_2$ samples with optimum Eu^{3+} concentration, under 465 nm excitation is shown in the Fig. 14 ((a) and (b) respectively). Correlated color temperature in kelvin scale, a unique property of solid state lighting devices, is used to characterize emitted light. CCT is calculated from color coordinates (x, y) using McCamy method[57] as

$$\mathrm{CCT} = -449n^3 + 3525n^2 - 6823.3n + 5520.33 \quad (7)$$

where $n = (x - x_e)/(y - y_e)$. Here (x_e, y_e), found as (0.3320, 0.1858), is the epicenter of convergence of isotemperature lines in 1931 CIE chromaticity diagram and n is the reciprocal of slope of line connecting (x, y) and (x_e, y_e). Color purity of luminescence of the phosphors is determined using

$$\text{Color purity} = \sqrt{\frac{(x - x_i)^2 + (y - y_i)^2}{(x_d - x_i)^2 + (y_d - y_i)^2}} \times 100\% \quad (8)$$

where (x_i, y_i) and (x_d, y_d) are the chromaticity coordinates of white illuminant (0.333, 0.333) and of dominant wavelength in the emission respectively.[58] Considering samples with optimum Eu^{3+} concentration, color purity of emission enhances from 89% to 94.7% when the substitution site of Eu^{3+} changes from single to double.

Photoluminescence life time measurements demonstrate the dynamics of down conversion in Eu^{3+} ions. The photoluminescence decay curves for $^5D_0 \rightarrow {}^7F_2$ transition (615 nm) of the prepared SL$_1$ and SL$_2$ phosphors under 465 nm excitation is

Table 5 Color coordinates, correlated color temperature and color purity calculated from emission spectra under 465 nm excitation for $Sr_{0.8-x}Eu_xLi_{0.2}Ti_{0.8}Nb_{0.2}O_3$ (SL_1) and $Sr_{0.8-x/2}Eu_xLi_{0.2}Ti_{0.8-x/2}Nb_{0.2}O_3$ (SL_2) phosphors

	SL_1: $Sr_{0.8-x}Eu_xLi_{0.2}Ti_{0.8}Nb_{0.2}O_3$				SL_2: $Sr_{0.8-x/2}Eu_xLi_{0.2}Ti_{0.8-x/2}Nb_{0.2}O_3$			
	Color coordinates				Color coordinates			
Value of x	x	y	CCT (kelvin)	Color purity (%)	x	y	CCT (kelvin)	Color purity (%)
0.08	0.64	0.36	1994	88.6	0.65	0.35	2266	92.2
0.12	0.64	0.36	1994	89.0	0.66	0.34	2634	94.7
0.16	0.64	0.36	1994	89.0	0.66	0.34	2634	94.5

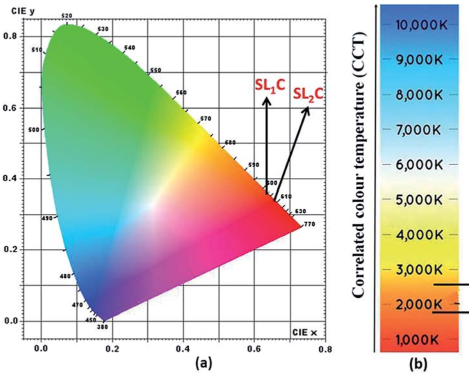

(a) (b)

Fig. 14 (a) CIE chromaticity diagram and (b) correlated color temperature diagram of $Sr_{0.68}Eu_{0.12}Li_{0.2}Ti_{0.8}Nb_{0.2}O_3$ (SL_1c) and $Sr_{0.74}Eu_{0.12}Li_{0.2}Ti_{0.74}Nb_{0.2}O_3$ (SL_2c).

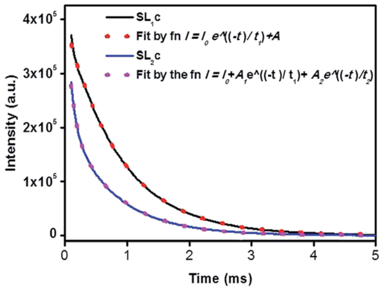

Fig. 15 The photoluminescence decay curves for $^5D_0 \rightarrow {}^7F_2$ transition (615 nm) of $Sr_{0.68}Eu_{0.12}Li_{0.2}Ti_{0.8}Nb_{0.2}O_3$ (SL_1c) and $Sr_{0.74}Eu_{0.12}Li_{0.2}Ti_{0.74}Nb_{0.2}O_3$ (SL_2c) under 465 nm excitation, fitted by single and double exponential functions respectively.

shown in the Fig. S9 ((a) and (b) respectively).† Decay curves of phosphors with optimum Eu^{3+} concentration, SL_1c and SL_2c, fitted with exponential functions are given in Fig. 15. All the transients of SL_1 are fitted well with the single exponential decay function as,

$$I = I_0\, e^{\frac{-t}{\tau}} + A \tag{9}$$

where I, I_0 and τ are intensity at time t, intensity at time zero and decay time respectively and A is a constant. The fitting parameters of PL decay curves of SL_1 phosphors are represented in Table 6. The single exponential nature of decay curves of these A-site doped phosphors indicates the presence of single activator site in the host matrix.[1] The lifetime of $^5D_0$ excited state is determined by radiative and non-radiative decay rates. Phosphor which has least non-radiative energy transfer shows longest life time.

However luminescence decay curves of $Sr_{0.8-x/2}Eu_xLi_{0.2}Ti_{0.8-x/2}Nb_{0.2}O_3$ (SL_2) phosphors shown in the Fig. S9(b)† are fitted well with the double exponential function,

$$I = I_0 + A_1 e^{\frac{-t}{\tau_1}} + A_2 e^{\frac{-t}{\tau_2}} \tag{10}$$

where τ_1 and τ_2 are the life time values of activator ions occupying two sites of dissimilar crystallographic environments and A_1 and A_2 are constants.[1,15] The average decay time can be calculated as

$$\tau_{av} = \frac{A_1\tau_1{}^2 + A_2\tau_2{}^2}{A_1\tau_1 + A_2\tau_2} \tag{11}$$

The relative ratio factor is calculated as

$$R_i = \frac{A_i}{\sum\limits_i A_i} \tag{12}$$

The fitting parameters are shown in Table 7. The presence of two life time values indicates the existence of two types of Eu^{3+} activator ions. According to phonon frequency concept, for optimum doping concentration, 45% of total population occupying relatively higher symmetric site of Sr^{2+} are long lived species with life time 0.765 ms. The other 55% of Eu^{3+} ions, short lived species with life time 0.092 ms resides at the lower symmetric site of Ti^{4+}.[6,59,60] It is found that as the concentration of europium in the samples increases, the population of long lived species decreases. While looking at the values of life time reported, one should take into account the fact that the life time of Eu^{3+} ions at different sites of Sr^{2+} and Ti^{4+} ions will be

Table 6 The fitting parameters of PL decay curves of $Sr_{0.8-x}Eu_xLi_{0.2}Ti_{0.8}Nb_{0.2}O_3$ (SL_1)

Value of x	τ (ms)	I_0	A
0.08	0.826(1)	314(9)	53 789(12)
0.12	0.875(1)	492(7)	395 720(23)
0.16	0.841(1)	283(8)	70 804(15)

Table 7 The fitting parameters of PL decay curves of $Sr_{0.8-x/2}Eu_xLi_{0.2}Ti_{0.8-x/2}Nb_{0.2}O_3$ (SL_2)

Value of x	τ_1 (ms)	τ_2 (ms)	τ_{av} (ms)	A_1	A_2	R_1	R_2	I_0
0.08	0.765(1)	0.130(1)	0.708	25 957(12)	14 960(10)	0.63	0.37	127(8)
0.12	0.765(1)	0.092(1)	0.680	216 709(25)	260 628(32)	0.45	0.55	385(7)
0.16	0.720(1)	0.123(1)	0.604	37 755(10)	53 063(10)	0.42	0.58	154(4)

different and which in turn can make the average life time depending on the responsible number of host sites at which substitution was made.

3.2 Judd–Ofelt and radiative analysis

For assessing radiative properties, luminescence behavior and site symmetry of Eu^{3+} ions in SL_1 and SL_2 type phosphors, Judd–Ofelt intensity parameters were calculated for representative compositions. Judd–Ofelt theory[50,61] is used to determine the phenomenological parameters Ω_λ ($\lambda = 2, 4, 6$) by fitting experimental line strength data. The values of Judd–Ofelt intensity parameters are dependent on the lanthanide ion and largely independent on the host matrix producing the crystal field surrounding the ion. These values are important in systematizing lanthanide intensity data. The differences in the values of Ω_λ for a given lanthanide ion in different hosts can be attributed to differential ligand field effects associated with coordination numbers, coordination geometries and lanthanide–ligand interaction mechanisms.[62] They are important for investigating the local structure and bonding in the host where the rare earth ions are situated. Ω_2 is the most sensitive parameter to the local structure and the material composition, which determine the asymmetry and covalence of lanthanide ion.[63] But Ω_4 and Ω_6 parameters depend on bulk material properties like viscosity and dielectric constant. Usually Ω_2, Ω_4 and Ω_6 are determined from a least square fit to the experimental absorption intensities. Since the reduced matrix elements (RME), $U(2)$, $U(4)$ and $U(6)$ are non-zero only for the $^5D_0 \rightarrow {}^7F_2$, $^5D_0 \rightarrow {}^7F_4$, $^5D_0 \rightarrow {}^7F_6$ transitions respectively, J–O parameters of Eu^{3+} ion can be calculated from the observed transition rates with taking the magnetic dipole transition $^5D_0 \rightarrow {}^7F_1$ as the reference. This technique, first proposed by Krupke[64] using absorption spectrum is very useful to calculate J–O parameters in various hosts. But here we adopted the same method with a difference of calculating the parameters using the spontaneous decay rates and calculation procedure is shown in ESI.†[65] The values of Ω_6 could not be calculated, since $^5D_0$–$^7F_6$ emission was lower than minimum detection limit of spectrofluorometer used. The J–O parameters were then used to calculate the transition probabilities $A_{j'-j}$ of excited states. From these quantities, the radiative life time τ_r, branching ratio β_{0J}, luminescence quantum efficiency η and stimulated emission cross section σ_{0J} were found and listed in the table.

According to Judd–Ofelt theory, the spontaneous radiative decay rate A_r, corresponding to the electronic transition in Eu^{3+} ions from an excited state $^5D_0$ to the final state ^7F_J can be calculated using,

$$A_r = A_{ED} + A_{MD} = \frac{64\pi^4\nu^3}{3h(2J+1)}(\chi_{ED}S_{ED} + \chi_{MD}S_{MD}) \tag{13}$$

where ν is the wave number associated with the transition, h the Planck constant, χ the local field correction for the effective field induced by the host lattice and S the line strength of the electronic transition involved.[66] The spontaneous radiative decay rate has a cubic dependence with the energy gap between the levels $^5D_0$ and ^7F_J. The larger the frequency of emitting radiation, larger will be the radiative emission rate. For electric dipole (ED) transitions,

$$\chi_{ED} = \frac{n(n^2+2)^2}{9} \tag{14}$$

$$\mathrm{SED} = e^2 \sum_\lambda \Omega_\lambda \left|\langle {}^5D_0 \| U^{(\lambda)} \| {}^7F_J \rangle\right|^2 \tag{15}$$

where $\lambda = 2, 4, 6$ and for magnetic dipole transitions,

$$\chi_{MD} = n^3 \tag{16}$$

$$S_{MD} = {\mu_B}^2 |\langle {}^5D_0 \| U^{(\lambda)} \| {}^7F_J \rangle|^2 \tag{17}$$

where n, the average refractive index was obtained as 2.21 and 2.17 for SL_1 and SL_2 samples respectively from reflection ellipsometry techniques. μ_B is the Bohr magneton and $|\langle {}^5D_0 || U^{(\lambda)} || {}^7F_J \rangle|^2$ are the reduced matrix elements (RME) of irreducible tensor operator of rank λ. Physically U^λ stands for electron repulsion and spin orbit coupling. The values of RME are host independent and have been reported by Carnall *et al.*[67,68] for various lanthanide ions. The electric dipole transitions within the 4f shell of a rare earth ion are possible only if its nucleus is not situated at the center of inversion. J–O parameter Ω_2 is very sensitive to the asymmetric neighborhood of Eu^{3+} ions. Ω_2 is found to increase with increase in concentration of Eu^{3+} in the prepared phosphors for both SL_1 and SL_2 samples with the latter has a large value in all the cases (Table 8). This indicates that the degree of increase in local asymmetry in the lattice with Eu concentration is at different rates for SL_1 and SL_2 type samples. The increase of value of Ω_2 from 3.67×10^{-20} cm^2 for A-site substituted sample to 4.80×10^{-20} cm^2 for A- and B-site substituted sample (for optimum doping concentration) is a direct evidence of increased local asymmetry in the system due to A- and B-sites substitution of Eu. This is also substantiated by Raman analysis. From the calculated values, we can find that $\Omega_2 > \Omega_4$. This shows the covalent nature of bonding between Eu^{3+} and host matrix.[58] The radiative life time τ_r of the emitting state $^5D_0$ is related to the spontaneous

Table 8 Judd–Ofelt intensity parameters (Ω_2, Ω_4) of $Sr_{0.8-x}Eu_xLi_{0.2}Ti_{0.8}Nb_{0.2}O_3$ (SL_1) and $Sr_{0.8-x/2}Eu_xLi_{0.2}Ti_{0.8-x/2}Nb_{0.2}O_3$ (SL_2) samples

	$Sr_{0.8-x}Eu_xLi_{0.2}Ti_{0.8}Nb_{0.2}O_3$			$Sr_{0.8-x/2}Eu_xLi_{0.2}Ti_{0.8-x/2}Nb_{0.2}O_3$		
Parameter	$x = 0.08$	$x = 0.12$	$x = 0.16$	$x = 0.08$	$x = 0.12$	$x = 0.16$
Ω_2 (10^{-20} cm^2)	3.60	3.67	3.39	4.58	4.80	4.78
Ω_4 (10^{-20} cm^2)	1.59	1.63	1.69	1.64	0.75	0.61

Table 9 Transition rates (A_R, A_{NR} and A_T), life time (τ_{rad} and τ_{obs}), emission quantum efficiency (η), branching ratios (β_{01}, β_{02}, β_{04}) and stimulated emission cross sections (σ_{01}, σ_{02} and σ_{04}) of $Sr_{0.8-x}Eu_xLi_{0.2}Ti_{0.8}Nb_{0.2}O_3$ and $Sr_{0.8-x/2}Eu_xLi_{0.2}Ti_{0.8-x/2}Nb_{0.2}O_3$ phosphors

	$Sr_{0.8-x}Eu_xLi_{0.2}Ti_{0.8}Nb_{0.2}O_3$			$Sr_{0.8-x/2}Eu_xLi_{0.2}Ti_{0.8-x/2}Nb_{0.2}O_3$		
Radiative parameter	$x = 0.08$	$x = 0.12$	$x = 0.16$	$x = 0.08$	$x = 0.12$	$x = 0.16$
A_R (s^{-1})	707	717	712	867	943	930
A_{NR} (s^{-1})	503	425.5	475.9	542.8	527.8	622
A_T (s^{-1})	1210	1140	1180	1410	1470	1650
τ_{rad} (ms)	1.41	1.39	1.40	1.15	1.06	1.08
τ_{obs} (ms)	0.826	0.875	0.841	0.708	0.680	0.604
η (%)	58.9	62.9	60.1	61.6	64.2	55.9
β_{01} (%)	23.2	22.8	23.0	20.6	18.6	19.5
β_{02} (%)	62.1	62.2	58.0	74.1	76.2	76.4
β_{04} (%)	13.1	13.2	13.8	3.28	4.31	2.70
σ_{01} (10^{-23} cm^2)	20.7	19.8	19.6	27.8	35.6	37
σ_{02} (10^{-22} cm^2)	7.93	8.02	8.09	7.67	8.19	7.2
σ_{04} (10^{-23} cm^2)	3.4	3.71	3.55	3.71	2.96	1.92

emission probabilities for all transitions from this state to the low lying ^7F_J states,

$$\tau_r = \frac{1}{\sum_J A_r(J' \to J)} \tag{18}$$

The observed luminescence life time of the state $^5D_0$ is

$$\tau_{obs} = \frac{1}{A_R + A_{NR}} \tag{19}$$

Quantum efficiency is the ratio of number of photons emitted to number of photons absorbed by the system and is given by,

$$\eta = \frac{\tau_{obs}}{\tau_r} \tag{20}$$

In estimating quantum efficiency, for $Sr_{0.8-x}Eu_xLi_{0.2}Ti_{0.8}Nb_{0.2}O_3$, single value of life time, τ alone is to be taken into account but for $Sr_{0.8-x/2}Eu_xLi_{0.2}Ti_{0.8-x/2}Nb_{0.2}O_3$, τ_1 and τ_2 are to be considered and the observed changes in quantum yield are attributed to population of ions at different sites A- and B- and the respective lifetimes. The fluorescence branching ratio which gives the relative contribution of each transition from the excited state to a final state can be determined as

$$\beta_{0J} = \frac{A_{0J}}{\sum_J A_{0J}} \tag{21}$$

where $J = 1, 2, 4$. The highest branching ratio is found for $^5D_0 \rightarrow {}^7F_2$ emission, as this is the dominant emission line, responsible for red color. The peak stimulated emission cross section for the transition $^5D_0 \rightarrow {}^7F_J$ is related to the radiative transition probability as

$$\sigma_{0J} = \frac{{\lambda_p}^4 A_{0J}}{8\pi c n^2 \Delta\lambda_{eff}} \tag{22}$$

where λ_p is the peak wave length of emission transition and $\Delta\lambda_{eff}$ is the effective line width of the emission band. The highest stimulated emission cross section obtained for $^5D_0 \rightarrow {}^7F_2$ emission indicating that it is the most efficient transition. The calculated J–O parameters and radiative parameters (Table 9) are at par with the reported values for Eu^{3+} ions.[10,49,50,56]

4. Conclusions

In summary, this work proposes a new series of $SrTiO_3$:$LiNbO_3$ perovskite solid solution host lattices to derive ample Eu^{3+} luminescence, under both UV (395 nm) and blue (465 nm) irradiations. Three series of red emitting phosphors $Sr_{0.95-x}Eu_{0.05}Li_xTi_{1-x}Nb_xO_3$, $Sr_{0.8-x}Li_{0.2}Ti_{0.8}Nb_{0.2}O_3$:$x$$Eu^{3+}$ and $Sr_{0.8-x/2}Li_{0.2}Ti_{0.8-x/2}Nb_{0.2}O_3$:$x$$Eu^{3+}$ were prepared using conventional high temperature solid state reaction. The photoluminescence intensity and asymmetric ratio of $^5D_0 \rightarrow {}^7F_2$ to $^5D_0 \rightarrow {}^7F_1$ transitions of $SrTiO_3$:Eu^{3+} phosphor were highly sensitive to $LiNbO_3$ incorporation. In this work an attempt was made to understand the effect of Eu^{3+} substitution at A-sites (Sr^{2+}) and at A- and B-sites (Sr^{2+} and Ti^{4+}) simultaneously. High resolution transmission electron micrographs showed the crystalline nature of the samples and elemental X-ray dot mapping images confirmed the homogeneous distribution of constituent elements in the phosphor samples. The site selective substitution was analyzed using techniques such as X-ray diffraction, Raman spectroscopy and luminescence life time measurements. We found that when the substitution was made simultaneously at A- and B-sites to produce $Sr_{0.8-x/2}Li_{0.2}Ti_{0.8-x/2}Nb_{0.2}O_3$:$x$$Eu^{3+}$, the color purity was found to increase from 89 to 94.7% along with the enhancement in intensity of red emission by 1.46 times with respect to that of A site substituted $Sr_{0.8-x}Li_{0.2}Ti_{0.8}Nb_{0.2}O_3$:$x$$Eu^{3+}$. The change in unit cell volume obtained from Rietveld refinement of X-ray diffraction patterns and the increase in intensity of first order TO_2, TO_4 and LO_4 vibrational modes and the first order *R*-point vibrations in the Raman shifts confirmed the site selected substitutions of Eu^{3+} ions. The double exponential luminescence decay curves of $Sr_{0.8-x/2}Li_{0.2}Ti_{0.8-x/2}Nb_{0.2}O_3$:$x$$Eu^{3+}$ and the existence of slow decaying Eu^{3+} ions having 0.765 ms life time with 45% occupancy and fast decaying Eu^{3+} ions having 0.092 ms life time with 55% occupancy (for optimum dopant concentration) also clearly evidenced the simultaneous substitution at A- and B-sites. The critical distance between dopant ions for energy transfer was found to be 17.74 and 18.06 Å for A-sites doped and A- and B-sites doped phosphors respectively. Increase in asymmetric ratio was observed due to decrease in local symmetry around Eu^{3+} ions, and this observation was in good agreement with the increase in value of the intensity parameter Ω_2 obtained from Judd–Ofelt analysis. The results indicate that $Sr_{0.8-x}Li_{0.2}Ti_{0.8}Nb_{0.2}O_3$:$x$$Eu^{3+}$ can act as a promising red phosphor in a variety of applications by exciting either at 395 or at 465 nm. In addition, the proposed site selective substitution can further improve its color purity and intensity.

Acknowledgements

G. Jyothi acknowledges University Grants Commission (UGC), India for the award of teacher fellowship under faculty development programme. The authors acknowledge Dr P. Prabhakar Rao, Chief Scientist and Head, Materials Science Division, CSIR-National Institute for Interdisciplinary Studies and Technology, Thiruvananthapuram, India for his valuable help in performing Rietveld analysis.

References

1 K. Li, X. Liu, Y. Zhang, X. Li, H. Lian and J. Lin, *Inorg. Chem.*, 2015, **54**, 323–333.

2 E. Downing, L. Hesselink, J. Ralston and R. Macfarlane, *Science*, 1996, **273**, 1185–1189.

3 S.-P. Lee, S.-D. Liu, T.-S. Chan and T.-M. Chen, *ACS Appl. Mater. Interfaces*, 2016, **8**, 9218–9223.

4 S. K. Mahesh, P. P. Rao, M. Thomas, T. L. Francis and P. Koshy, *Inorg. Chem.*, 2013, **52**, 13304–13313.

5 S. Saha, S. Das, U. K. Ghorai, N. Mazumder, D. Ganguly and K. K. Chattopadhyay, *J. Phys. Chem. C*, 2015, **119**, 16824–16835.

6 S. K. Gupta, a. K. Yadav, D. Bhattacharya, S. N. Jha and V. Natarajan, *J. Lumin.*, 2015, **164**, 1–22.

7 Q. Zhang, H. Sun, T. Kuang, R. Xing and X. Hao, *RSC Adv.*, 2015, **5**, 4707–4715.

8 J. Boltersdorf, B. Zoellner, C. M. Fancher, J. L. Jones and P. A. Maggard, *J. Phys. Chem. C*, 2016, **120**, 19175–19188.

9 M. Sletnes, M. Lindgren, J. C. Valmalette, N. P. Wagner, T. Grande and M. A. Einarsrud, *J. Solid State Chem.*, 2016, **237**, 72–80.

10 R. Shukla, S. K. Gupta, V. Grover, V. Natarajan and A. K. Tyagi, *Dalton Trans.*, 2015, **44**, 10628–10635.

11 C. Jiang, L. Fang, M. Shen, F. Zheng and X. Wu, *Appl. Phys. Lett.*, 2009, **94**, 2007–2010.

12 H. Zhan, Z.-G. Chen, J. Zhuang, X. Yang, Q. Wu, X. Jiang, C. Liang, M. Wu and J. Zou, *J. Phys. Chem. C*, 2015, **119**, 3530–3537.

13 A. Durán, E. Martínez, J. A. Díaz and J. M. Siqueiros, *J. Appl. Phys.*, 2005, **97**, 104109.

14 A. Tkach, P. M. Vilarinho, D. Nuzhnyy and J. Petzelt, *Acta Mater.*, 2010, **58**, 577–582.

15 F. Kang, M. Peng, X. Yang, G. Dong, G. Nie, W. Liang, S. Xu and J. Qiu, *J. Mater. Chem. C*, 2014, **2**, 6068.

16 D. Wang, T. Kako and J. Ye, *J. Phys. Chem. C*, 2009, **113**, 3785–3792.

17 L. Tsonev, *Opt. Mater.*, 2008, **30**, 892–899.

18 L. Xing, Y. Xu, R. Wang, W. Xu, S. Gu and X. Wu, *Chem. Phys. Lett.*, 2013, **577**, 53–57.

19 E. P. Smirnova, A. V. Sotnikov, N. V. Za, M. Weihnacht and V. V. Lemanov, *Phys. Solid State*, 2008, **50**, 122–125.

20 Y. Tsur, T. D. Dunbar and C. A. Randall, *J. Electroceram.*, 2001, **7**, 25–34.

21 J. Shi, J. Ye, L. Ma, S. Ouyang, D. Jing and L. Guo, *Chem.–Eur. J.*, 2012, **18**, 7543–7551.

22 Y. G. Abreu, J. C. Soares, R. L. Moreira and A. Dias, *J. Phys. Chem. C*, 2016, **120**, 16960–16968.

23 P. R. Arya, P. Jha and A. K. Ganguli, *J. Mater. Chem.*, 2003, **13**, 415–423.

24 J. Y. Dai, W. P. Chen, G. K. H. Pang, P. F. Lee, H. K. Lam, W. B. Wu, H. L. W. Chan and C. L. Choy, *Appl. Phys. Lett.*, 2003, **82**, 3296.

25 W. Luo, Z. Li, X. Jiang, T. Yu, L. Liu, X. Chen and Z. Zou, *Phys. Chem. Chem. Phys.*, 2008, **3**, 6717–6723.

26 G. Bhaskar Kumar and S. Buddhudu, *Phys. B*, 2008, **403**, 4164–4170.

27 W. Li, L. Ning and P. A. Tanner, *J. Phys. Chem. A*, 2012, **116**, 7337–7344.

28 U. Balachandran and N. G. Eror, *J. Am. Ceram. Soc.*, 1982, **65**, c54–c56.

29 S. Qin, X. Wu, F. Seifert and A. I. Becerro, *J. Chem. Soc., Dalton Trans.*, 2002, 3751–3755.

30 A. Grzechnik, G. H. Wolf and P. F. McMillan, *J. Raman Spectrosc.*, 1997, **28**, 885–889.

31 F. A. Rabuffetti, H.-S. Kim, J. A. Enterkin, Y. Wang, C. H. Lanier, L. D. Marks, K. R. Poeppelmeier and P. C. Stair, *Chem. Mater.*, 2008, **20**, 5628–5635.

32 R. L. Moreira, R. P. S. M. Lobo, G. Subodh, M. T. Sebastian, F. M. Matinaga and A. Dias, *Chem. Mater.*, 2007, **19**, 6548–6554.

33 J. Hlinka, J. Petzelt, S. Kamba, D. Noujni and T. Ostapchuk, *Phase Transitions*, 2006, **79**, 41–78.

34 M. D. Fontana, G. Metrat, J. L. Servoin and F. Gervais, *J. Phys. C: Solid State Phys.*, 1984, **17**, 483–514.

35 A. E. Souza, G. T. A. Santos, B. C. Barra, W. D. Macedo, S. R. Teixeira, C. M. Santos, A. M. O. R. Senos, L. Amaral and E. Longo, *Cryst. Growth Des.*, 2012, **12**, 5671–5679.

36 P. Jayabal, V. Sasirekha, J. Mayandi, K. Jeganathan and V. Ramakrishnan, *J. Alloys Compd.*, 2014, **586**, 456–461.

37 D. Hreniak, A. Speghini, M. Bettinelli and W. Strek, *J. Lumin.*, 2006, **119**, 219–223.

38 M. N. Iliev, M. L. F. Philips, J. K. Meen and T. M. Nenoff, *J. Phys. Chem. B*, 2003, **107**, 14261–14264.

39 M. P. F. Graça, M. A. Valente, M. Peres, A. Cruz, M. J. Soares, A. J. Neves, T. Monteiro, L. C. Alves and E. Alves, *J. Phys.: Condens. Matter*, 2007, **19**, 16213.

40 A. Slodczyk, M.-H. Limage, P. Colomban, O. Zaafrani, F. Grasset, J. Loricourt and B. Sala, *J. Raman Spectrosc.*, 2011, **42**, 2089–2099.

41 S. Som, P. Mitra, V. Kumar, V. Kumar, J. J. Terblans, H. C. Swart and S. K. Sharma, *Dalton Trans.*, 2014, **43**, 9860.

42 E. Orhan, F. M. Pontes, M. A. Santos, E. R. Leite, A. Beltrán, J. Andrés, T. M. Boschi, P. S. Pizani, J. A. Varela, A. Carlton, A. Taft and E. Longo, *J. Phys. Chem. B*, 2004, **108**, 9221–9227.

43 G. Blasse and B. C. Grabmaier, *Luminescent Materials*, Springer Berlin Heidelberg, Berlin, Heidelberg, 1994.

44 A. Ling Li and S. Zhang, *J. Phys. Chem. B*, 2006, **110**, 21438–21443.

45 C. R. García, J. Oliva, M. T. Romero, R. Ochoa-Valiente and L. A. G. Trujillo, *Adv. Mater. Sci. Eng.*, 2015, **2015**, 1–7.

46 Y. F. Wu, Y. T. Nien, Y. J. Wang and I. G. Chen, *J. Am. Ceram. Soc.*, 2012, **95**, 1360–1366.

47 P. J. Zeng, L. P. Yu, Z. X. Qiu, J. L. Zhang, C. Y. Rong, C. Z. Li, Z. H. Fu and S. X. Lian, *J. Sol-Gel Sci. Technol.*, 2012, **64**, 315–323.

48 Y. Su, L. Li and G. Li, *Chem. Mater.*, 2008, **20**, 6060–6067.

49 G. Blasse, *Spectra and Chemical Interactions*, Springer Berlin Heidelberg, Berlin, Heidelberg, 1976, pp. 43–79.

50 B. R. Judd, *Phys. Rev.*, 1962, **127**, 750–761.

51 B. Marí, K. C. Singh, P. Cembrero-Coca, I. Singh, D. Singh and S. Chand, *Displays*, 2013, **34**, 346–351.

52 J. Liu, H. Lian and C. Shi, *Opt. Mater.*, 2007, **29**, 1591–1594.

53 W. Ran, L. Wang, L. Tan, D. Qu and J. Shi, *Sci. Rep.*, 2016, **6**, 27657.

54 H. J. S. Fuping Du, Y. Nakai, T. Tsuboi and Y. Huang, *J. Mater. Chem.*, 2011, 4669–4678.

55 G. Blasse, *Philips Res. Rep.*, 1969, **24**, 131–144.

56 R. W. G. Hunt, *Measuring Colour: Applied Science and Industrial Technology*, Ellis Horwood, New York, 2nd edn, 1991.

57 C. S. McCamy, *Color Res. Appl.*, 1992, **17**, 142–144.

58 R. G. A. Kumar, S. Hata, K. Ikeda and K. G. Gopchandran, *RSC Adv.*, 2016, **6**, 67295–67307.

59 S. K. Gupta, C. Reghukumar and R. M. Kadam, *RSC Adv.*, 2016, **6**, 53614–53624.

60 S. K. Gupta, P. S. Ghosh, N. Pathak, a. Arya and V. Natarajan, *RSC Adv.*, 2014, **4**, 29202.

61 G. S. Ofelt, *J. Chem. Phys.*, 1962, **37**, 511.

62 E. M. Stephens, S. Davis, M. F. Reid and F. S. Richardson, *Inorg. Chem.*, 1984, **23**, 4607–4611.

63 Ä. Andresen, A.-N. Bahar, D. Conradi, I.-I. Oprea, R. Pankrath, U. Voelker, K. Betzler, M. Wöhlecke, U. Caldiño, E. Martín, D. Jaque and J. G. Solé, *Phys. Rev. B: Condens. Matter Mater. Phys.*, 2008, **77**, 214102.

64 W. F. Krupke, *Phys. Rev.*, 1966, **145**, 325–337.

65 L. Liqin and C. Xueyuan, *Nanotechnology*, 2007, **18**, 255704.

66 M. J. Weber, T. E. Varitimos and B. H. Matsinger, *Phys. Rev. B: Solid State*, 1973, **8**, 47–53.

67 W. T. Carnall, H. Crosswhite and H. M. Crosswhite, *Argonne Natl. Lab. Report*, Argonne, IL, USA, 1978.

68 W. T. Carnall, P. R. Fields and K. Rajnak, *J. Chem. Phys.*, 1968, **49**, 4450.